

Hydrodynamics of Lock-exchange Turbidity Currents down a Slope Based on Direct Numerical Simulation

Liang Zhao, Chinghao Yu, Ying-Tien Lin, Peng Hu, Xiaolong Liang, Zhiguo He*
(Ocean College, Zhejiang University, 310058, Hangzhou, China)
(*Corresponding author, E-mail: hezhiguo@zju.edu.cn)

Abstract: Turbidity currents play a vital role in various geophysical environments. However, until now, few studies have taken into the effects of both suspended particle and slope on its evolution, which requires a precise information of the spatio-temporal flow field. Hence, this study presents high-resolution and two-dimensional direct numerical simulations (DNS) of lock-exchange turbidity currents down a slope. By analyzing front velocity, water entrainment, and energy budget, the factors that affect the driving force, thus the development of the turbidity current, are detailedly investigated. The front velocity history exhibits three distinct stages over time, i.e., a short acceleration stage, a quasi-constant stage, and a deceleration stage. The calculation of the entrainment ratio shows that the mixing due to the collapse of the dense fluid is much stronger than that due to the Kelvin–Helmholtz instabilities and turbulent billows. For a turbidity current down a slope, the entrainment volume of ambient water decreases as the particle size increases, which is contrary to the situation of the turbidity current on a flat bed. This is because the increase effect of the larger front velocity exceeds the decrease effect of the stronger stratification to the entrainment volume of ambient water. However, the change of the particle size has little effect on the entrainment ratio. The analysis of the energy budget exhibits that the potential energy is rapidly converted into the kinetic energy in the initial time period. Later then, most of the energy is dissipated. The increase of the slope angle leads to a more rapid energy transition process from the potential energy to the kinetic and the dissipated energy.

Key words: Direct numerical simulation; Turbidity current; Slope; Particle; Entrainment; Energy Budget.

1. Introduction

A gravity current is the flow driven by the density difference between the fluid and the ambient environment^[1]. When the density difference is caused by suspended particles in the current, it is also called a turbidity current, which often occurs in both natural and engineering situations. In the estuary and ocean, it transports a large amount of sediment from the river to the deep sea^[2, 3]. In the reservoir, it is

responsible for the sedimentation and the storage capacity loss^[4]. In the engineering practice, even a small turbidity current could destroy the underwater instruments due to its strong impact^[5]. Because of its significant importance in a wide range of flow phenomenon, extensive studies on gravity and turbidity currents have been carried out by experiment, modeling, and field investigation in the past several decades.

The previous experimental results^[2, 6] demonstrated that the full lock-exchange gravity current would go through several well-defined phases after starting from a rest state due to the different controlling forces. A relative short acceleration phase appeared firstly after gravity current was generated, which was followed by a slumping phase characterized by nearly constant front velocity. When the balance was reached between the inertial force and the buoyancy force, it came into the self-similar phase with the front velocity as a function of $t^{-1/3}$. Later on, the viscous force became dominated with the decrease of inertial force and the current enters into the viscous-buoyancy phase, which leads the front velocity as a function of $t^{-4/5}$. However, for the lock-exchange gravity current down a slope, the experimental results^[7-9] indicated that the gravity current firstly experienced an acceleration stage and then followed by a deceleration stage. Recently, the simulation results^[10, 11] showed a nearly constant stage of the front velocity could also appear between the acceleration and the deceleration stages in the lock-exchange condition. It has been proved that the slope can notably influence the front velocity of the gravity current^[1] as it brings a component of the gravitational force along the slope. In the case of the turbidity current, the existence of the phases mentioned above is determined not only by the slope^[1], but also by the properties of the suspended particles^[5]. If the turbidity current is formed by coarse particles, the flow could settle down before the viscous-buoyancy phase because most of the particles have deposited. On the contrary, the flow could develop into the viscous-buoyancy phase if the particles are smaller and keep suspended for a longer time^[12]. However, few studies have taken into account the effect of both particle and slope on the development of the lock-exchange turbidity current. To gain an intensive understanding of its evolution, it is necessary to recognize the role that particle and slope play during its advancement process.

Theoretically, the main driving force of the gravity current is the density contrast between the current and the ambient fluid. The density contrast would decrease due to the continuous mixing and entrainment with the ambient lighter fluid. Based on the

experimental results of the constant-inflow gravity currents, the entrainment ratio E was determined to be a function of the Richardson number Ri ^[13], given by

$$E = \frac{0.08 - 0.1Ri}{1 + 5Ri}. \quad (1)$$

The empirical expression of Eq. (1) is valid for $0 \leq Ri \leq 0.8$ and has been widely adopted by many researchers^[14-16] to determine the entrainment ratio of both gravity and turbidity currents. This entrainment ratio was experimentally measured to be about 0.04 around the turbulent/non-turbulent interface in terms of small-scale and constant-inflow aspects with the slope up to 10° ^[16]. However, for the lock-exchange gravity current, different entrainment dynamics was exhibited as the current can not be fed by the constant dense fluid from the source. Hallworth et al.^[17] determined the entrainment ratio of the lock-exchange gravity current over a flat bed as 0.063 ± 0.003 by a neutralization technique, which agreed well with the value calculated by their theoretical model. For the lock-exchange gravity current flowing down a slope in the range of $5^\circ \leq \theta < 90^\circ$, the experimental results of Beghin et al.^[7] indicated that the entrainment ratio had a nearly linear relationship with the slope angle θ . For the lock-exchange gravity current, with the flow propagating along the slope, remarkably unsteady characteristics, such as the front velocity, the turbulent structure, and the interface instability, can be detected over time, which intensely influence the entrainment ratio. As a result, the above experimental results of the entrainment ratio can only be treated as the bulk value. This was further proved by the study of Nogueira et al.^[18], in which strong temporal variations of the entrainment ratio of lock-exchange gravity current on a flat bed were observed. Mostly recently, Ottolenghi et al. numerically studied the entrainment ratio of lock-exchange gravity current propagating on flat bottom^[19] and up slope^[20], respectively, which also showed the great temporal variations of the entrainment ratio. Since the previous studies of the entrainment ratio of lock-exchange gravity and turbidity current down a slope are mainly focused on the bulk value, the assessment of the time evolution of the mixing and entrainment effect in this strongly unsteady current down a slope is still an outstanding question, which requires a detailed knowledge of the spatio-temporal flow field.

From the viewpoint of the energy, the propagation of gravity current essentially involves the energy transformation, in which the initial potential energy is converted

to the kinetic energy and the dissipated energy. In the case of the turbidity current, the situation is more complicated by the fact that the dissipated energy also includes the part arisen from the microscopic Stokes flow around the particles^[21]. Hence, the detailed information of the flow field is needed to investigate the energy budget, which is difficult to be obtained experimentally due to the limit of the instruments. Alternatively, various numerical models have been conducted to simulate the gravity and turbidity currents in different environments. The main simulation methods can be divided into the depth-averaged model^[2, 14, 15] and the depth-resolving model^[2]. The later one usually includes the Reynolds-Averaged Navier-Stokes simulation (RANS)^[22-25], the Large-Eddy Simulation (LES)^[26-30], and the Direct Numerical Simulation (DNS)^[21, 31, 32] (A detailed review can be found in [Ref. 2015](#)). As one of the most accurate depth-resolving models, DNS can provide the high-resolution results of the spatial and temporal information of the flow field. Härtel et al.^[31] carried out the first DNS to simulate the lock-exchange gravity current. They focused on the influence of the boundary condition and the lobe-and-cleft instability on the head of gravity current. Necker et al.^[21] investigated the influence of the particle deposition on the flow dynamics of the lock-exchange turbidity current by DNS. Later on, Necker et al.^[32] further used the same method to study the energy budget and the mixing process during the evolution of the lock-exchange turbidity current. They found that the sedimentation of the particles was responsible for about 50 % of all energy losses and the larger settling velocity could lead to the more intense mixing^[32]. Liu and Jiang^[33] numerically checked the effect of the boundary condition and initial depth of the dense fluid on the lock-exchange gravity current. They found that the effect of the top boundary would be different with the change of the release depth ratio. The above studies applying the DNS to simulate the gravity and turbidity currents were all conducted on a flat bottom which ignored the impact of bed topography. In the real geophysical situation, the bottom condition is much more complicated, which can greatly affect the characteristics of the gravity and turbidity currents. Blanchette et al.^[34] considered the influence of the resuspended particles on the self-sustaining turbidity current by a DNS method. Dai^[10, 11, 35] carried out the DNS of the lock-exchange gravity current over a slope. He mainly focused on the front velocity of the particle-free gravity current and the numerical simulations were compared with the results derived from the thermal theory. Nasr-Azadani et al.^[36, 37] simulated the

bi-disperse turbidity current over a three-dimensional Gaussian bump. Their simulation results showed the particles with different size were deposited in the different position of the bump^[36]. They also proposed a scaling law to determine the maximum bump height that the turbidity current could surmount^[37]. In summary, quite a few previous studies have investigated the features of the gravity and turbidity currents on a flat bottom by DNS method, including the front velocity^[21], the energy budget^[32, 38], and the mixing process^[32]. The influences of the boundary condition^[31, 33], particle sedimentation^[12, 21], and the Reynolds number^[38] are also considered in these studies. On the other hand, the previous experimental and numerical results show the gravity and turbidity currents down a slope behaves differently from that on a flat bottom^[1, 5, 7, 10]. For the lock-exchange currents, one of the greatest characteristics is the unsteady features over time. Open issues still appear in the time evolution of front velocity, entrainment ratio, and energy budget of the lock-exchange turbidity current descending a slope. It is meaningful to understand the advancement of the turbidity current down a slope, and the role of the influence factors, such as the Reynolds number, particle size, and the slope angle in this process.

Therefore, the purpose of this study is to provide detailed insight into the hydrodynamics of lock-exchange turbidity current down a slope under different parameters, including the Reynolds number, the settling velocity of the particle (particle size), and the slope angle. A high-resolution DNS solver with the fifth-order accuracy is proposed to simulate lock-exchange turbidity currents down a slope. With the help of the high-resolution information of the flow field over time, special attentions are paid on the front velocity, the energy budget, and the entrainment ratio of the turbidity current. This paper is organized as follows. The numerical model, including the governing equations, boundary conditions, and numerical scheme, is introduced firstly. Then, the model is validated by comparing the simulation results with the experimental data published in the literature. Later, we present the detailed simulation results obtained from the DNS model. Finally, some conclusions are drawn and suggestions for the future study are given.

2. Numerical model

In this paper, the parameter with a $\hat{\quad}$ sign means it is dimensional, while the parameter without a $\hat{\quad}$ sign means it is nondimensional. The sketch view of the computational domain is shown in Fig. 1. Here we consider the situation that the

volume fraction of the particles in the turbidity current is relatively low so the interactions between the particles can be neglected^[21, 32]. The coupling between the fluid and the particle is determined by the momentum transfer^[21]. The motion of the fluid phase is described by the Navier-Stokes equations with the Boussinesq approximation^[32]:

$$\frac{\partial \hat{u}_i}{\partial \hat{x}_i} = 0, \quad (2)$$

$$\frac{\partial \hat{u}_i}{\partial \hat{t}} + \hat{u}_i \frac{\partial \hat{u}_i}{\partial \hat{x}_i} = -\frac{1}{\hat{\rho}} \frac{\partial \hat{p}}{\partial \hat{x}_i} + \hat{\nu} \frac{\partial^2 \hat{u}_i}{\partial \hat{x}_i \partial \hat{x}_i} + \hat{c} \frac{(\hat{\rho}_p - \hat{\rho})}{\hat{\rho}} e_i^g \hat{g}, \quad (3)$$

where \hat{u}_i is the fluid velocity, \hat{t} is the time, $\hat{\rho}$ is the density of the fluid, \hat{p} is the pressure, $\hat{\nu}$ is the kinematic viscosity, \hat{c} is the volume fraction of the particle, $\hat{\rho}_p$ is the density of the particle which is assumed to be much larger than the density of the fluid, and $e_i^g = (0, 0, -1)$ is the vector in the gravity direction.

The concentration field of the particle is described by a transport equation^[21, 32]

$$\frac{\partial \hat{c}}{\partial \hat{t}} + \hat{u}_{p,i} \frac{\partial \hat{c}}{\partial \hat{x}_i} = \hat{k} \frac{\partial^2 \hat{c}}{\partial \hat{x}_i \partial \hat{x}_i}, \quad (4)$$

where \hat{k} is the diffusion coefficient, \hat{u}_s is the settling velocity of the particle, and $\hat{u}_{p,i}$ is the velocity of the particle. Here we assume that the velocity of the particle were the sum of the fluid velocity and the setting velocity of the particle^[21, 32]:

$$\hat{u}_{p,i} = \hat{u}_i + e_i^g \hat{u}_s. \quad (5)$$

The setting velocity of the particle is determined by^[37]

$$\hat{u}_s = \frac{\hat{d}_p^2 (\hat{\rho}_p - \hat{\rho}) \hat{g}}{18 \hat{\mu}}, \quad (6)$$

where \hat{d}_p is the diameter of the particle, and $\hat{\mu}$ is the dynamic viscosity of the fluid.

To make the above governing equations dimensionless, the length scale is chosen as the half height of the initial particle-laden fluid $\hat{h}/2$. The velocity scale is chosen as the buoyancy velocity \hat{u}_b ^[37]

$$\hat{u}_b = \sqrt{\frac{\hat{h} (\hat{\rho}_p - \hat{\rho})}{2 \hat{\rho}} \hat{g} \hat{c}_0}, \quad (7)$$

where \hat{c}_0 is the initial volume fraction of the particles within the lock (see Fig. 1, the gray area). The time scale is $\hat{h}/2\hat{u}_b$ and the pressure scale is $\hat{\rho}\hat{u}_b^2$. Taking these characteristic scales into the above equations, we can get the nondimensional governing equations

$$\nabla \cdot u_i = 0, \quad (8)$$

$$\frac{\partial u_i}{\partial t} + (u_i \cdot \nabla) u_i = -\nabla p + \frac{1}{Re} \nabla^2 u_i + c e_i^g, \quad (9)$$

$$\frac{\partial c}{\partial t} + (u_i + u_s e_i^g) \cdot \nabla c = \frac{1}{ReSc} \nabla^2 c. \quad (10)$$

where the volume concentration of the particles is normalized by \hat{c}_0 . Re is the Reynolds number, which is defined as:

$$Re = \frac{\hat{u}_b \hat{h} / 2}{\hat{\nu}}. \quad (11)$$

Sc is the Schmidt number, which represents the ratio of viscosity to the diffusivity:

$$Sc = \frac{\hat{\nu}}{\hat{k}}. \quad (12)$$

If $Sc \geq 1$, its influence on the turbidity current can be neglected^[21] so Sc is set to be unity as many previous studies did^[10, 21, 32].

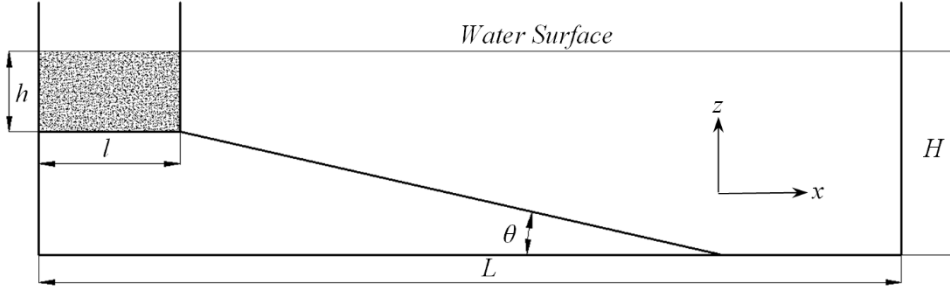


Fig. 1. Sketch view of the two-dimensional lock-exchange turbidity current down a slope. The initial particle-laden fluid is confined in the shade region $l \times h$. The length and height of the computational domain are L and H , respectively. The angle of the slope is θ .

For the velocity boundary condition, free-slip boundary is applied at the top ($z = H$). No-slip boundary is applied at the bottom ($z = 0$) and side walls ($x = 0, L$), that is $u_i = 0$. For the concentration field boundary condition, the no-flux boundary condition is implemented at the top^[37]:

$$u_s c + \frac{1}{ScRe} \frac{\partial c}{\partial z} = 0. \quad (13)$$

In this way, we can ensure that no particle can be transported through the top boundary. At the side walls, the no-flux boundary condition is achieved by^[37]

$$\frac{\partial c}{\partial x} = 0. \quad (14)$$

At the bottom boundary, the particle is assumed to leave the flow due to sedimentation, which is numerically achieved by^[21]

$$\frac{\partial c}{\partial t} = u_s \frac{\partial c}{\partial z}. \quad (15)$$

In this study, as the concentration of the particles is relatively low so we do not consider the resuspension of the particles and the change of the bottom due to the sedimentation of the particles^[21].

The governing equations are solved in the following procedures. The initial discontinuous concentration field is smoothed by solving initialization equation introduced by Osher and Fedkiw^[39]. The concentration field is prescribed unity in the gray area (see Fig. 1) and zero elsewhere with a distance function in the interface. The approximate spatial derivative term in the distance function is solved by the scheme of fifth-order weighted essentially non-oscillatory (WENO5)^[40]. The spatial derivative term is approximated by a combined compact difference scheme. The discontinuous concentration field is solved by combined compact difference (CCD) algorithm^[41]. For the momentum equation, we adopt a sixth-order upwinding combined compact difference scheme to approximate the first-order derivative terms^[41]. The convection and diffusion terms are solved simultaneously and efficiently by twin-forward elimination and two-backward substitution solution solver^[41]. Then, a two-step projection method^[42] is applied: firstly, an intermediate velocity which does not fully satisfy the divergence-free condition is computed by ignoring the pressure gradient term. Afterwards, the intermediate velocity is corrected by solving pressure Poisson equation using the Gauss-Seidel iteration solver to obtain the final solution. An immersed boundary condition with virtual force is implemented in the boundary along the slope^[43].

3. Validation of the numerical model

Following the previous study, the accuracy of the numerical model is validated by comparing the data of the front location from the simulations to that from the corresponding experiments^[34]. The front location X_f is defined as the distance from

the foremost of the current, which can be determined by a threshold value of the particle concentration 0.01, to the start point of the slope (see Fig. 3 (d) in [next section](#)). The configuration of the tank that Kubo used in his lock-exchange experiments of turbidity currents down a slope^[44] is similar with the one in our simulation. As a result, the data from Kubo's experiments are adopted to validate our numerical model. Here we give a brief introduction of the experiments for convenience and completeness.

Two groups of data of the front location are available in the paper of Kubo, i.e., Experiment B1 and Experiment B5. The experiments were conducted in a 10 m long, 0.2 m wide and 0.5 m deep flume. The siliceous particles with a representative density of 2650 kg/m³ were well mixed in tap water as the initial dense fluid. The settling velocity of the particles had a mid value of 5.5×10^{-3} m/s. The initial volume fraction of these particles was 2 %, which is sufficiently low that the interactions between the particles can be neglected^[44]. In Experiment B1, the length and height of the initial area filled with particle-laden fluid (see Fig. 1, the gray area) were 0.5 m and 0.2 m, respectively. The depth of the ambient lighter water was 0.4 m. The horizontal length of the slope was 2 m. In Experiment B5, the length and height of the initial area filled with particle-laden fluid were 0.5 m and 0.2 m, respectively. The depth of the ambient lighter water was 0.3 m. The horizontal length of the slope was 1 m. With these data, we can calculate the non-dimensional parameters applied in the corresponding simulations, as summarized in Table 1.

Table 1. The non-dimensional parameters in the experiments and the corresponding simulations. N_L and N_H mean the numbers of the mesh in the x and z direction, respectively. N.E. means the relevant parameters do not exist.

Case	$\tan(\theta)$	h	l	L	H	u_s	Re	$N_L \times N_H$
Exp_B1	0.1	2	5	100	4	0.03	17865	N.E.
Sim_B1	0.1	2	5	26	4	0.03	3000	1430 \times 220
Exp_B5	0.1	2	5	100	3	0.03	17865	N.E.
Sim_B5	0.1	2	5	16	3	0.03	3000	880 \times 165

There are two non-dimensional parameters that are different in the experiment and the corresponding simulation case, i.e., the length of computational domain L and the Reynolds number Re . The previous research^[34] demonstrated that if distance between the foremost of the turbidity current and the right wall was larger than one non-dimensional length, the features of the flow would not be affected by the choice

of L . As a result, the value of L in the simulation case is set to be much smaller than the value in corresponding experiments but also fulfil the requirement of the one non-dimensional length to save the computational effect. In such simulations, the spatial resolution should meet the requirement that the size of the grid is of the order $O(1/(ReSc)^{0.5})$ ^[10, 45]. To save the computational effort, the value of Re is 3000 in the simulation case, which is much smaller than the value 17865 in the corresponding experiment. The previous study^[34] proved that the characteristics of the gravity currents were nearly independent of Re when $Re > 1000$. Besides, as will be seen in the **below section**, our analysis also conformed this conclusion. The choices of L and Re here will not change the final simulation results.

The comparisons of the front location measured experimentally by Kubo^[44] with the value from our simulations are shown in Fig. 2. Since we only care about the features of the gravity currents on the slope in this study, the comparison is made within the distance over the slope. Some tiny discrepancies appear in the initial time period, in which the experimental values are a little larger than the simulated results. This difference is attributed to the extra energy injection into the initial particle-laden fluid from the stirring to keep the particles suspended. The satisfactory agreements demonstrate that the present two-dimensional numerical model can well reproduce the evolution of the turbidity currents over the distance of the whole slope.

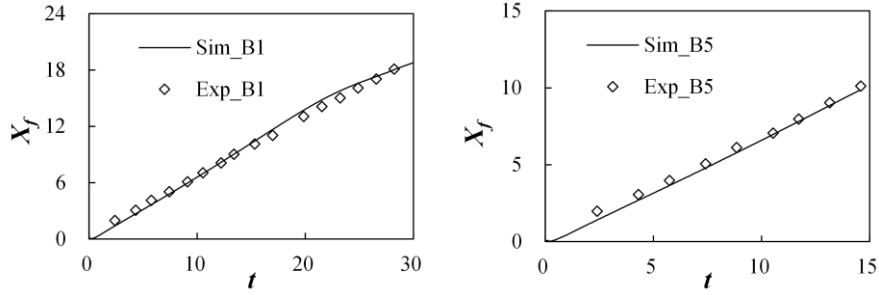


Fig. 2. Comparison of the front location measured experimentally by Kubo^[44] with the value from our simulations.

4. Simulation results

4.1. Development of the turbidity current

The simulation cases in this study are presented in Table 2. The controlling parameters include the slope angle, the setting velocity of the particle and the Reynolds number. We describe the characteristics of the turbidity current down a slope from the representative case, i.e., case 3, $\theta = 10^\circ$, $u_s = 0.02$ and $Re = 3000$. The analysis in the **next section (Section)** demonstrates that the Reynolds number has little

effect on the features of the gravity current when $Re > 1000$. As a result, the case that $Re = 3000$ is chosen here.

Table 2. The simulation cases in this study

Case	slope ($^{\circ}$)	h	l	L	H	u_s	Re	$N_L \times N_H$
1	0	2	1	16	4	0.02	3000	880×220
2	6	2	1	24	4	0.02	3000	1320×220
3	10	2	1	16	4	0.02	3000	880×220
4	15	2	1	16	4	0.02	3000	880×220
5	10	2	1	16	4	0.02	500	880×220
6	10	2	1	16	4	0.02	800	880×220
7	10	2	1	16	4	0.02	1000	880×220
8	10	2	1	16	4	0	3000	880×220
9	10	2	1	16	4	0.005	3000	880×220
10	30	2	1	16	4	0.02	3000	880×220

Fig. 3 shows the time evolution of the turbidity current down a slope in case 3. Once the lock is released, the heavy fluid starts to collapse forward, as shown at $t = 1$. At this time, the head of the turbidity current has not formed. Within the initial short time period, the evolution of the turbidity current is mainly controlled by this collapse process. Later on, as the dense fluid continues to flow down, a clear head structure is then developed from $t \approx 1.4$. At the lower interface between the turbidity current and the slope, a lifted nose is formed. At the upper interface between the turbidity current and the ambient water, a velocity-shear layer is generated, which promotes the Kelvin–Helmholtz instabilities and turbulent billows. Besides, as time goes on, a raising cloud emerges at the tail part of the current. These structures at the upper interface dominantly determine the properties of the turbidity current in the later stage. Fig. 4 shows the velocity field and the streamlines of the turbidity current at $t = 6$. In the main body of the current, the velocity vectors and the streamlines uniformly appear. However, in the part where the Kelvin–Helmholtz instabilities, the turbulent structures and the raising cloud exist, the velocity vectors irregularly grow and the smaller streamline circles develop. These structures generate mixing at the interface and the ambient clear water is entrained into the descending current^[25]. The density of the turbidity current is reduced by this mixing and entrainment as well as the setting of the particles. At the later time, the descending current starts to dissipate ($t = 15$) as its density largely decreases. It can be inferred that the density contrast would persistently decrease as the particles continuously settle down. The turbidity current

would finally die out by the viscous effect.

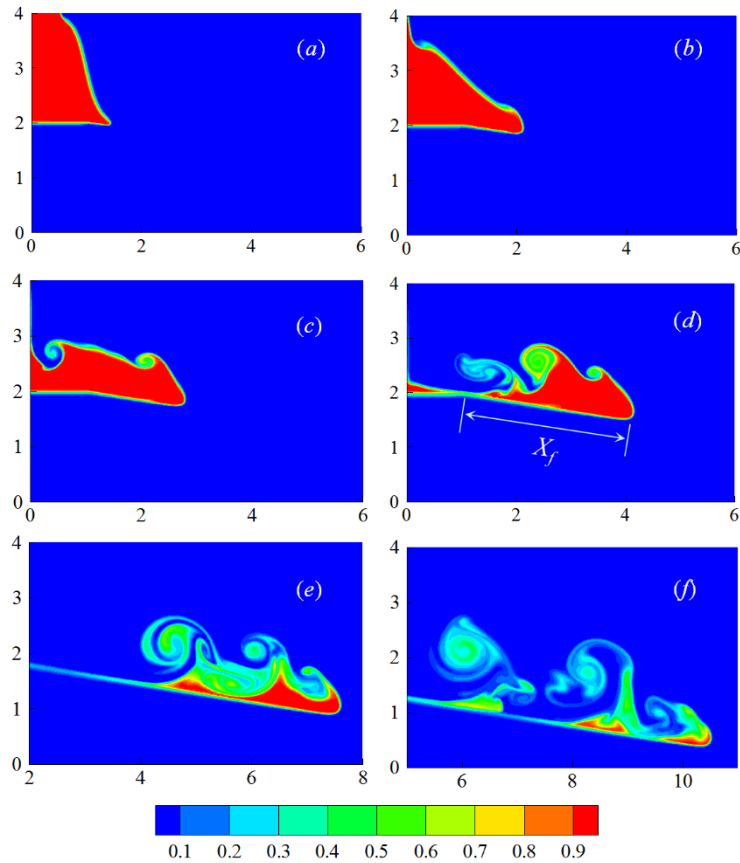


Fig. 3. Time evolution of turbidity current down a 10° slope. $Re = 3000$. The turbidity current is visualized by the contour of the particle concentration. (a) $t = 1$; (b) $t = 2$; (c) $t = 3$; (d) $t = 5$; (e) $t = 10$; (f) $t = 15$.

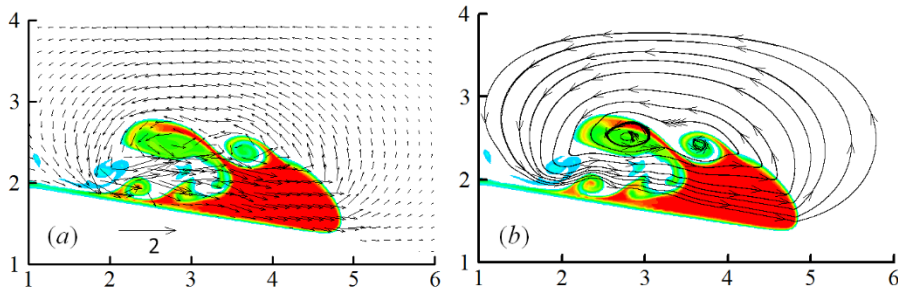


Fig. 4. (a) The velocity field, and (b) Streamline of the turbidity current down a 10° slope at $t = 6$. $Re = 3000$.

Fig. 5 shows turbidity currents down different slopes at $t = 6$. The basic characteristics of the turbidity currents, i.e., the lifted nose at the lower interface and the turbulent billows at the upper interface, still appear with the variation of the slopes. However, as the slope angle increases, the length of the turbidity current head becomes shorter and its height gets larger. Besides, the two main turbulent billows at the upper interface present a tendency to become more complex. When the slope angle increases to 30° , the two billows are even mixed together and a larger cloud is

then formed. The change in the shape indicates that the mixed region of the turbidity current increases as the slope angle increases. To demonstrate this conclusion quantitatively, following the previous study^[10], the mixed region is defined as the area where the particle concentration is in this range

$$0.1 < c < 0.9. \quad (16)$$

The time evolution of the area of the mixed region in different cases are presented in Fig. 6. In the initial acceleration stage during which the turbidity current is mainly controlled by the collapse process, the mixed region is not sensitive to the change of the slope angle. While in the later stages, the increase of the slope angle makes the area of the mixed region grow more quickly. This conclusion agrees with the previous numerical study of the gravity current^[10]. However, it is more accurate to evaluate the mixing and entrainment effect by the dimensionless parameter, i.e., the entrainment ratio^[46], which is not only related to the mixed area, but also to the front velocity of the current. In the next section, a detailed analysis of the front velocity is presented.

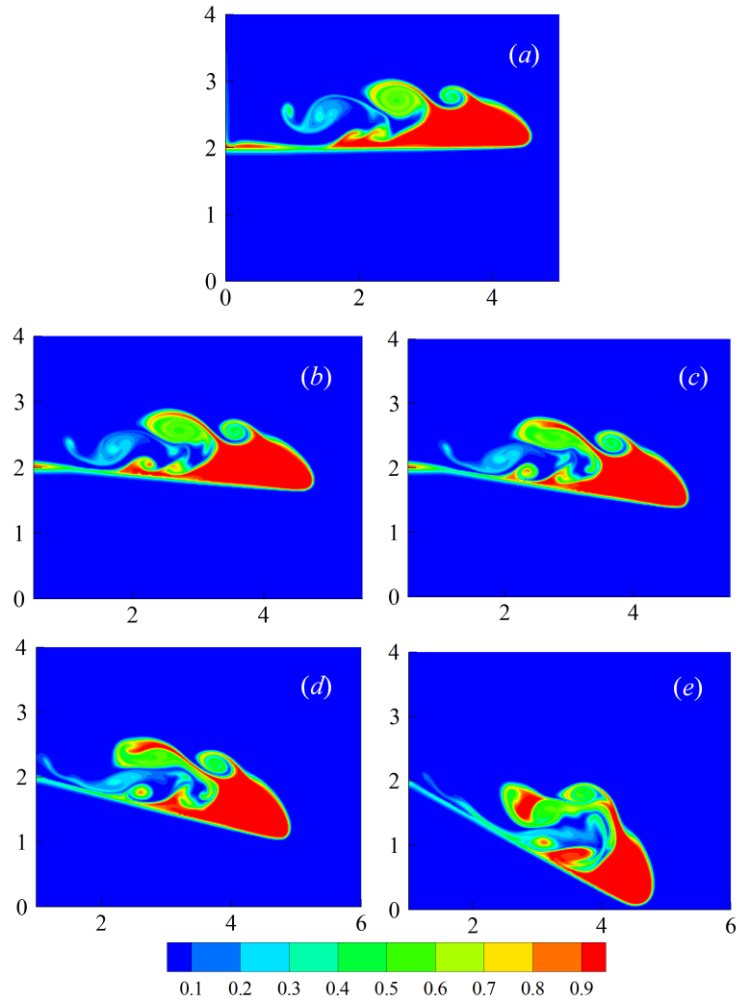


Fig. 5. Turbidity currents down different slope angles at $t = 6$. (a) $\theta = 0^\circ$; (b) $\theta = 6^\circ$; (c) $\theta = 10^\circ$; (d) $\theta = 15^\circ$; (e) $\theta = 30^\circ$.

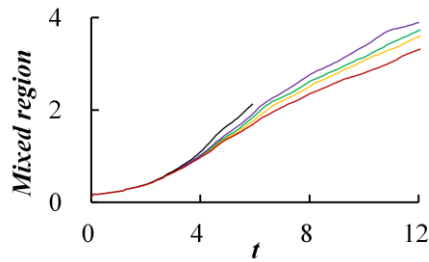


Fig. 6. Time evolution of the mixed region of turbidity currents down different slope angles. $Re = 3000$. —, $\theta = 0^\circ$; —, $\theta = 6^\circ$; —, $\theta = 10^\circ$; —, $\theta = 15^\circ$; —, $\theta = 30^\circ$.

4.2. Front velocity

It is well known that the development of the gravity current on a flat bottom can be divided into the acceleration, slumping, inertia-buoyancy and buoyancy-viscous stages^[2], during which the front velocity of the current behaves differently. For the turbidity current down a slope, both the slope and the particle can influence its evolution. In our simulation, the front velocity U_f can be calculated by $U_f = dX_f / dt$.

Fig. 7 shows the typical time evolution of the front velocity from $t = 0$ to $t = 18$, by which time the turbidity current has arrived at the end of the slope. Based on the behavior of U_f over time, the development of the turbidity current down a slope can be divided into three distinct stages. From $t = 0$ to $t \approx 1.3$, as the density contrast between the turbidity current and the ambient water is relatively large, the sudden collapse of the dense fluid in the initial area leads to a short acceleration stage of the turbidity current, during which the front velocity increases rapidly from zero to the maximum value $U_{fmax} \approx 0.66$. After $t \approx 1.3$, the front velocity keeps a nearly constant value 0.64, which means the turbidity current is experiencing a quasi-constant stage. In this stage, a temporary balance is reached between the negative effects, including the mixing with the ambient clear water and the setting of the particles, which reduce the driving force, and the positive effect, i.e., the component of the reduced gravitational force along the slope, which increases the driving force. Since the density contrast constantly decreases, the component of the reduced gravitational force is not large enough to make up the negative effects. The turbidity current enters into the next deceleration stage at $t \approx 9.5$ and the front velocity begins to decrease. If the slope were long enough, the density contrast would finally vanish and the turbidity current would eventually stop its movement. On the contrary, the deceleration stage would be missed if the slope were not so long.

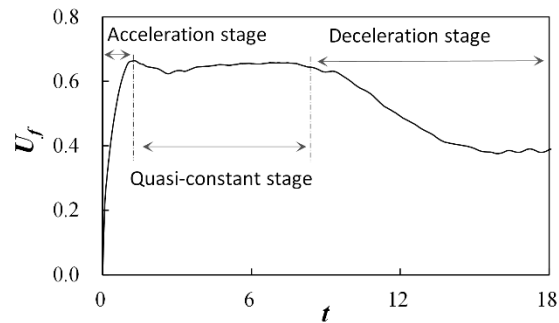


Fig. 7. The front velocity of the turbidity current down a 10° slope. $Re = 3000$.

4.2.1. Influence of the Reynolds number

Fig. 8 shows the time evolution of the front velocity of turbidity currents with different Re . For the relatively small Reynolds number, $Re < 1000$, the front velocity increases quickly with Re except for in the initial acceleration stage, where U_f is not affected by Re . This dependence relationship of U_f on Re can be neglected for $Re > 1000$, where the values of U_f are almost the same when $Re = 1000$ and 3000. This conclusion can also be seen in the previous study of the gravity current^[34]. For the

adequately large Re , other characteristics of the turbidity current, such as the head structure and the number of the main eddies, are also not influenced by Re . This means that the cases with $Re = 3000$ can well describe the hydrodynamics of the turbidity current down a slope.

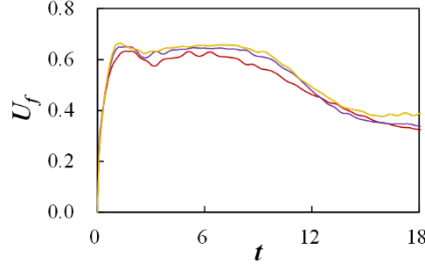


Fig. 8. Time evolution of front velocity of turbidity currents down a slope with different Re . $\theta = 10^\circ$. —, $Re = 500$; —, $Re = 800$; —, $Re = 1000$; —, $Re = 3000$.

4.2.2. Influence of the settling velocity

The density difference between the current and the ambient water is originally due to that the current contains suspended particles. In this study, the mass of the suspended particles m_s is calculated by

$$m_s(t) = \int_{\Omega} c(t) \cdot dV . \quad (17)$$

Fig. 9 shows the mass of the suspended particles and the front velocity of turbidity currents down a slope. The settling velocity 0, 0.005 and 0.02 corresponds to the compositional gravity current, the turbidity current with fine suspended particles and the turbidity current with coarse suspended particles. It presents that the turbidity current with coarse particles loses particles more quickly. As a result, the driving force reduces more quickly and its front velocity also has a smaller value. However, the size of the particle has little effect on U_f in the initial acceleration stage, during which the movement of the turbidity current is dominated by the collapse of the particle-laden fluid. In the later stage, as more coarse particles settle out, the velocity difference between the currents gets larger.

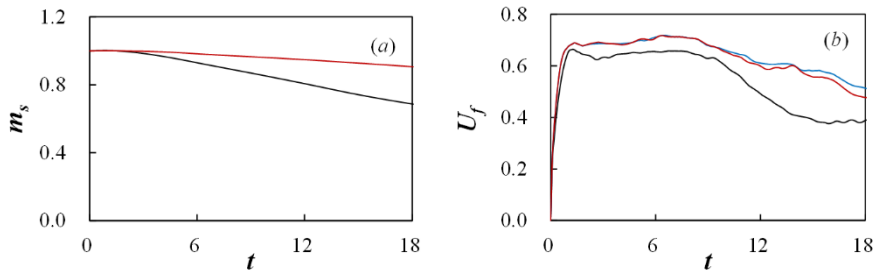


Fig. 9. Time evolution of (a) the mass of the suspended particles, and (b) the front velocity of turbidity currents with different settling velocity down a slope. $Re = 3000$. —, $u_s = 0$; —, $u_s = 0.005$; —, $u_s = 0.02$.

0.02.

4.2.3. Influence of the slope angle

Fig. 10 shows the time evolution of the front velocity of turbidity currents down different slopes. The front velocity in the case $\theta = 30^\circ$ is recorded from $t = 0$ to $t = 6$, at that time the turbidity current has arrived at the end of the slope. It can be seen the short acceleration stage is not sensitive to the change of slopes. The influence of the slope on the front velocity reflects in the later quasi-constant stage. When $\theta = 0^\circ$, the front velocity slightly decreases about 11 % in this relatively long period stage. When $\theta = 6^\circ$ and 10° , the front velocity keeps a nearly fixed value 0.64 in this stage. However, the front velocity increases about 10 % in the quasi-constant stage for the case of $\theta = 15^\circ$. When the slope angle increases to 30° , the increase tendency of the front velocity in the quasi-constant stage becomes more obvious. Therefore, it can be concluded that the tendency of the front velocity in the quasi-constant stage alters from the slight decrease to minor increase with the increase of the slope angle.

For the movement of a turbidity current, the existence of the slope can bring an additional positive effect which drives its running, that is, the component of the reduced gravitational force along the slope. The interplay of the positive effect and the negative effect (mixing and particle settling) results in the presented behavior of the front velocity in the quasi-constant stage. For the turbidity current on a flat bottom, the slight decrease of U_f is due to that the negative effect exceeds the positive effect a little. The positive effect becomes larger with the increase of the slope angle. When the slope angle is within the range of 6° and 10° , a temporary balance is reached between the positive and negative effect. As the slope angle gets larger, the positive effect gradually surpasses the negative effect. Consequently, U_f is altered to a tendency of the minor increase.

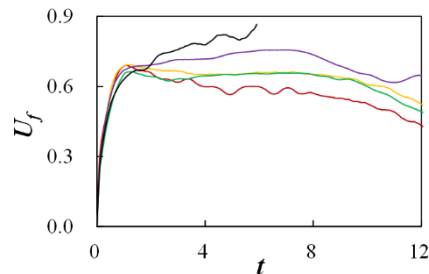


Fig. 10. Time evolution of front velocity of turbidity currents down different slope angles. $Re = 3000$. —, $\theta = 0^\circ$; —, $\theta = 6^\circ$; —, $\theta = 10^\circ$; —, $\theta = 15^\circ$; —, $\theta = 30^\circ$.

4.3. Entrainment ratio

Once the current starts to move due to the density difference, a velocity shear between the current and the ambient water exists. Kelvin–Helmholtz instabilities and turbulent billows are generated at the upper interface, making fluids with different densities mixed together. As the current evolves forward, the ambient lighter water is entrained into the current, which increases the volume of the current and decreases the density contrast. This effect in turn decreases its front velocity. Since the dynamics of the gravity and turbidity currents is greatly affected by this mixing and entrainment process, it is necessary to evaluate the entrainment ratio. In the present numerical model, as the particle phase is thought to have little effect on the total volume^[21, 32], the volume change of the turbidity current due to the particle setting can be neglected. The mixing and entrainment with the ambient water reflects in the time variation of the volume of the turbidity current^[19]. If the initial volume of the dense fluid is V_0 at $t_0 = 0$, by a successive time period Δt_i , the current has a larger volume $V_i = V_0 + \Delta V_i$ at $t_i = t_0 + \Delta t_i$. The bulk entrainment discharge can be calculated by^[19]

$$Q_{bulk,i} = \frac{\Delta V_i}{\Delta t_i}. \quad (18)$$

The volume of the turbidity current V_i is defined as the area where $c > 0.01$ in the present two-dimensional simulation. Although the volume is affected by the threshold value of c , it has been demonstrated that the mixing and entrainment effect is not significantly influenced when the value is within the range of 0.01 and 0.05^[20]. We can get the bulk entrainment velocity by^[19]

$$W_{bulk,i} = \frac{Q_{bulk,i}}{S_i}, \quad (19)$$

where S_i is the area of the interface between the current and the ambient water, which is very complexed to be determined due to the complicated structure at the interface area^[18, 19]. For simplicity, S_i is scaled by $S_i = (X_f + h + l)$ in the present two-dimensional simulation. Following the previous definition of the bulk entrainment ratio^[46], this was herein calculated by

$$E_{bulk,i} = \frac{W_{bulk,i}}{U_{f,i}}, \quad (20)$$

being $U_{f,i}$ the front velocity of the current at $t = t_i$ ^[47]. The local entrainment ratio $E_{local,i}$ can be calculated by the following expressions:

$$Q_{local,i} = \frac{V_i - V_{i-1}}{t_i - t_{i-1}}, \quad (21)$$

$$W_{local,i} = \frac{Q_{local,i}}{0.5(S_i + S_{i-1})}, \quad (22)$$

$$E_{local,i} = \frac{W_{local,i}}{0.5(U_{f,i} + U_{f,i-1})}. \quad (23)$$

4.3.1. Influence of the slope angle

The instantaneous entrainment and mixing effect leads to the change of the volume of the turbidity current, which is related to the variation of the local entrainment ratio^[19]. Fig. 11 shows the time evolution of E_{bulk} and E_{local} of turbidity currents down different slopes. Once the lock is released, the bulk entrainment ratio of the turbidity currents greatly drops from $t = 0$ to $t \approx 1.3$. This time period just exactly corresponds to the acceleration stage of the turbidity current, during which the movement of the turbidity current is dominated by the initial collapse process. After that, E_{bulk} keeps a nearly constant value of the order of 10^{-2} . Although the time evolution of E_{bulk} is similar to each other in all the simulations, the existence of the slope can bring a larger E_{bulk} , making more ambient lighter fluid entrained into the current. As the irregular entrainment and mixing happen at the upper interface between the current and the ambient water, the behavior of the local entrainment ratio is much more complicated. Here is an interesting coincidence that the presence of the slope leads to a peak value of E_{local} at $t \approx 1.3$, at which time the turbidity current also ends the acceleration stage, and E_{bulk} starts to keep nearly constant. The E_{local} of the turbidity current down a slope behaves more irregularly than that on a flat bottom, such as the existence of the three major peaks in the acceleration stage. In the later stage, the slope also makes more small peak values of E_{local} . As the size and intensity of the Kelvin–Helmholtz billows greatly affect E_{local} ^[19], the occurrence of these peak values reflects the influence of the slope on the instability of the turbidity current.

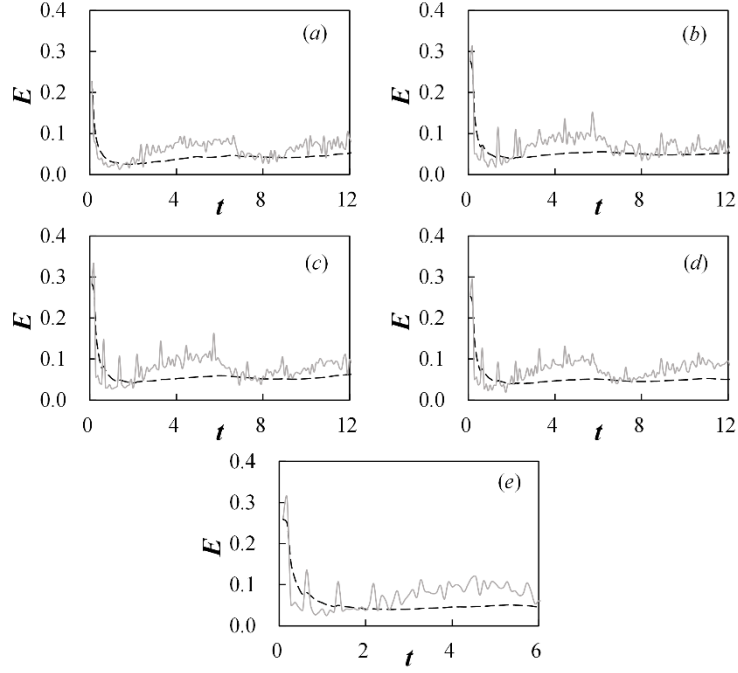


Fig. 11. Time evolution of entrainment ratio (gray line: E_{local} ; dotted line: E_{bulk}) of turbidity currents down different slopes. $Re = 3000$. (a) $\theta = 0^\circ$; (b) $\theta = 6^\circ$; (c) $\theta = 10^\circ$; (d) $\theta = 15^\circ$; (e) $\theta = 30^\circ$.

The analysis of the development of the turbidity current shows the dense fluid immediately starts to collapse forward after it is released from rest. This process is then followed by the propagation of the turbidity current down the slope, with Kelvin–Helmholtz instabilities and turbulent billows emerging at the upper interface. To understand the time variation of E_{local} thoroughly, we further analyze the structures of the turbidity current at $t = 1.36$, 3.27 , and 5.72 in case 3, when the peak values of E_{local} appear, as shown in Fig. 12. At $t = 1.36$, there is no obvious turbulent structure at the upper interface. The movement of the turbidity current is still dominated by the initial collapse process. The collapse of the dense fluid makes the ambient lighter water move along another direction, which causes the mixing and entrainment effect in this initial time period. Subsequently, as the turbidity current moves down the slope, the Kelvin–Helmholtz instabilities and turbulent billows start to develop at the upper interface. The vigorous time variation of E_{local} is exactly the result of this irregular development of these structures. The trajectories of the dense fluid within the current are curved by these structures and some of the dense fluid is raised into the ambient environment^[19]. When the stripes of the dense water are formed at the interface, ambient lighter water is engulfed into the current and the peak value of E_{local} appears, as shown in Fig. 12 (b) and (c). It is worth noting that the value of E_{local} in the initial time period is much larger than that in the later time. This means the mixing and

entrainment effect arising from the collapse of the dense fluid is much stronger than that from the Kelvin–Helmholtz instabilities and turbulent billows.

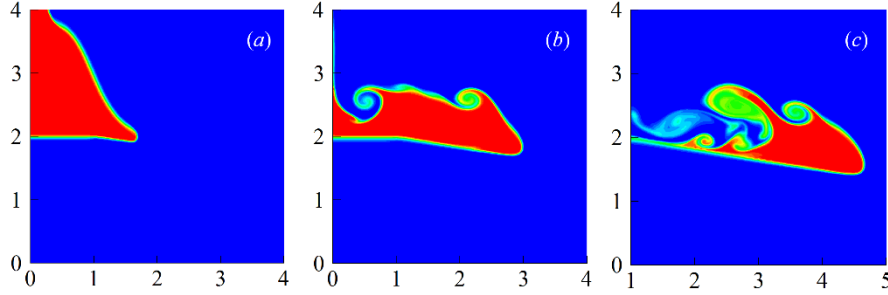


Fig. 12. The structures of the turbidity current at the time when the peak values of E_{local} appear in case 3. (a) $t = 1.36$; (b) $t = 3.27$; (c) $t = 5.72$.

4.3.2. Influence of the settling velocity

It is understandable that the current with a larger front velocity can entrain a larger volume of the ambient fluid. Besides, the intensity of the Kelvin–Helmholtz instabilities and the turbulence billows, which can be damped by the density stratification at the interface, can also influence the entrainment volume of the ambient fluid^[48]. The interplay of these factors renders the entrainment volume and entrainment ratio a complex problem. The recent study^[48] demonstrates that the entrainment volume of the ambient water of a turbidity current on a flat bed is greater than that of a gravity current, even though the gravity current has a larger front velocity. It is because that the sedimentation of the suspended particles makes the turbidity current have a weaker stratification at the interface than that of the gravity current^[48]. For a turbidity current, the increase effect of this weaker stratification exceeds the decrease effect of the smaller front velocity to the entrainment volume. Concerning a turbidity current down a slope, the problems of the entrainment volume and entrainment ratio are even more complicated as the slope can lead to a larger driving force for the turbidity current. Fig. 13 shows time evolution of volume, bulk entrainment ratio and local entrainment ratio of turbidity currents with different particles down a slope. It can be seen that the entrainment volume of the ambient water decreases as the particle size increases, which is contrary to the situation of the turbidity current on a flat bed. It should be noticed that the slope adds an additional driving force of the current, leading to a greater front velocity. For a turbidity current with finer particles down a slope, this greater front velocity is more obvious as the density contrast is larger than that of a turbidity current with coarse particles. Although the stronger stratification can decrease the intensity of the

Kelvin–Helmholtz and the turbulence vortices, and thus the entrainment volume of the ambient water, for a turbidity current with finer particles down a slope, the increase effect of the larger front velocity exceeds the decrease effect of the stronger stratification to the entrainment volume of the ambient water. On the other hand, the particle size has little effect on E_{bulk} and E_{local} of a turbidity current down a slope, which means the value of the entrainment ratio measured from a gravity current can be directly applied in the case of the turbidity current.

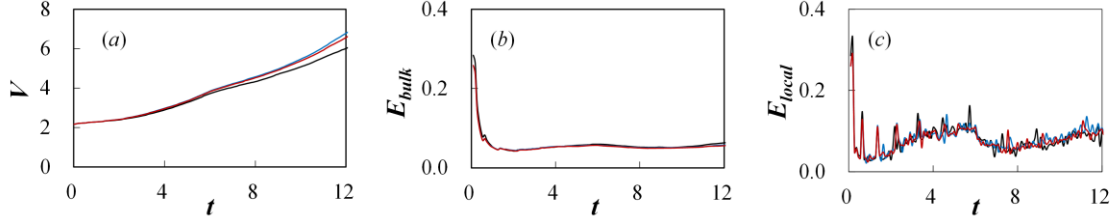


Fig. 13. Time evolution of (a) volume, (b) bulk entrainment ratio and (c) local entrainment ratio of turbidity currents with different setting velocity of the particle down a slope. $Re = 3000$, $\theta = 10^\circ$. —, $u_s = 0$; —, $u_s = 0.005$; —, $u_s = 0.02$.

4.4. Energy budget

Just as mentioned above, the movement of a turbidity current down a slope is essentially an energy transition process, in which the potential energy is converted into the kinetic energy and the dissipated energy due to the motions of the fluid and the particles. For a lock-exchange turbidity current, there is no energy input from the outer source. The current will finally die out because of the energy dissipation. At that time, the total dissipated energy should be equal to the initial available potential energy^[21]. In the experiments, it is very difficult to investigate the energy budget of the turbidity current by the limitation of the instruments^[2]. As the DNS solver can provide a detailed information of the flow field, the energy budget of the turbidity current can be obtained. The energy budget equation^[21] can be derived from Eqs. (9) and (10)

$$E_k(t) + E_p(t) = -\int_t (\varepsilon_f + \varepsilon_s) dt, \quad (24)$$

where $E_k(t)$ is the kinetic energy:

$$E_k(t) = \int_{\Omega} \frac{1}{2} u_i u_i dV. \quad (25)$$

$E_p(t)$ is the available potential energy:

$$E_p(t) = \int_{\Omega} c \cdot z dV. \quad (26)$$

Both the macroscopic convective motion of the fluids (ε_f) and the microscopic Stokes flow around each particle (ε_s) contribute to the energy dissipation, which can be derived from Eqs. (9) and (10)^[21]:

$$\varepsilon_f(t) = \int_{\Omega} \frac{2}{Re} s_{ij} s_{ij} dV, \quad (27)$$

$$\varepsilon_s(t) = \int_{\Omega} u_s \cdot c dV, \quad (28)$$

where s_{ij} is the rate-of-strain tensor:

$$s_{ij} = \frac{1}{2} \left(\frac{\partial u_i}{\partial x_j} + \frac{\partial u_j}{\partial x_i} \right). \quad (29)$$

Since the immersed boundary method is applied in our numerical scheme, the mass of the suspended particles reduces as some of these particles gradually settle out. This part of energy E_d contributes to the decrease of the total potential energy. It should also be accounted into the energy budget, which can be expressed by

$$E_d(t) = \int_x c_d(x,t) z(x) dx, \quad (30)$$

where $z(x)$ is the height z on the slope at the position x . $c_d(x,t)$ is the deposited concentration of the particles, which is expressed by

$$c_d(x,t) = \int_t u_s c(x, z(x), t) dt. \quad (31)$$

By introducing the total energy E_{tot} and the initial potential energy $E_p(0)$, the energy budget equation can be reconstructed into the following form

$$E_k(t) + E_p(t) + E_d(t) + E_f(t) + E_s(t) = E_{tot}(t) = const. = E_p(0). \quad (32)$$

where

$$E_f(t) = \int_t \varepsilon_f(t) dt \quad \text{and} \quad E_s(t) = \int_t \varepsilon_s(t) dt. \quad (33)$$

In Eq. (32), E_d is the part of the potential energy which can not be converted into the kinetic energy due to the settling out of the particles. From the viewpoint of the energy dissipation, it can also be regarded as part of the total energy loss. The total energy dissipation can be calculated by $E_{dis} = E_d + E_f + E_s$. Fig. 14 shows the time history of the six energy terms normalized by the initial available potential energy $E_p(0)$ in case 3. Based on Eq. (32), during the development of the turbidity current, the total energy should always keep a constant value 1. The simulation result in Fig.

14 demonstrates this tendency. The maximum variation of the total energy E_{tot} is about 2.2 %, which is resulted from the first-order scheme to compute these energy terms. In the whole process, the available potential energy E_p constantly decreases while the kinetic energy E_k continuously increases. In the first 3 time units, the change rate of E_p and E_k is much larger than that in the following time. In this short time period, the potential energy is rapidly converted into the kinetic energy. The turbidity current gets 71 % of its final kinetic energy (0.20 of 0.28) in 17 % of the total time (3 of 18). From $t = 3$ to $t = 18$, although the available potential energy decreases about 45 % of E_{tot} , the kinetic energy only increases about 8 % of E_{tot} , which means most of the potential energy is dissipated. For the present case, the energy dissipation resulted from the macroscopic flow and the microscopic Stokes flow is almost the same, which is about half of the value due to the settling out of the particles. When the turbidity current arrives at the end of the slope, about 42 % of the total energy is dissipated.

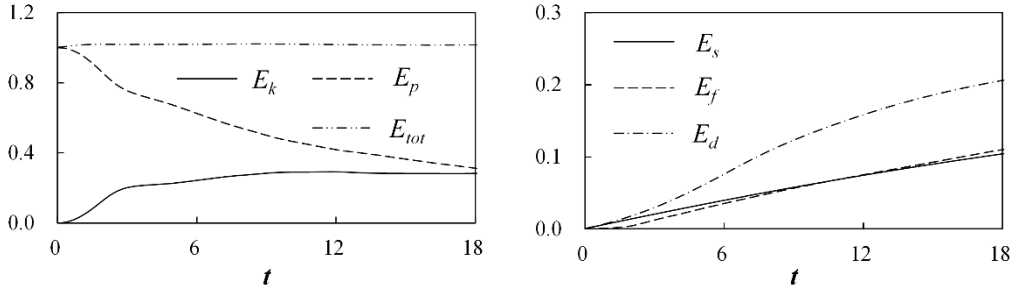


Fig. 14. Time evolution of the energy terms normalized by the initial available potential energy $E_p(0)$ in case 3.

4.4.1. Influence of the settling velocity

The influence of the settling velocity on the energy budget is investigated. Fig. 15 shows the time evolution of different energy terms of turbidity currents down a slope. In the initial time period, the flow is mainly controlled by the collapse of the dense fluids and most of the particles are still suspended. Hence, the change of the particle size has little effect on the E_k and E_p in this short time. Later on, although the change of the particle size does not alter the overall tendency of E_k , E_p and E_{dis} , clear discrepancies appear in these different energy terms. As the sedimentation of the particles results in an additional energy loss, the available potential energy and the kinetic energy in the gravity current are larger than that in the turbidity current at identical time. The discrepancies get greater when the differences between the particle sizes become larger. With the increase of the particle size, the available potential

energy drops more rapidly, making more energy dissipated and less energy converted into the kinetic energy.

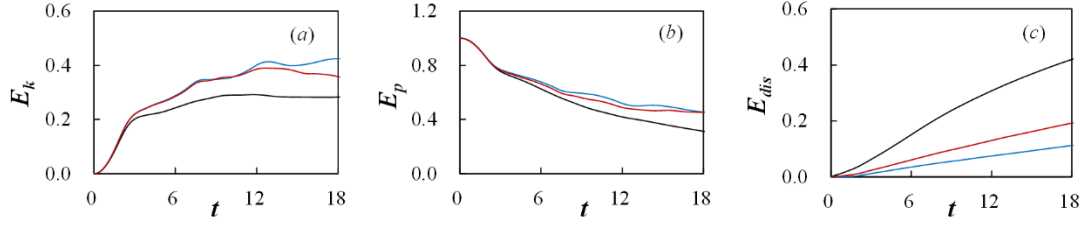


Fig. 15. Time evolution of (a) kinetic energy, (b) available potential energy and (c) dissipated energy of turbidity currents with different setting velocity of the particle down a slope. $Re = 3000$, $\theta = 10^\circ$. —, $u_s = 0$; —, $u_s = 0.005$; —, $u_s = 0.02$. These energy terms are normalized by the initial potential energy $E_p(0)$.

4.4.2. Influence of the slope angle

Fig. 16 shows the time evolution of kinetic energy E_k , available potential energy E_p and dissipated energy E_{dis} of turbidity currents down different slopes. For the turbidity current on a flat bottom, an energy conversion process from E_p to E_k rapidly happens in the first 3.5 time units, during which E_p drops about 25 % and E_k increases approximately 19 %, leaving 6 % of the total energy dissipated. After that, although E_p continues to decrease as the current propagates forward, E_k also starts to decay slowly, which means the turbidity current has come into an energy-dissipation stage. Comparing the turbidity current on a flat bed with that down a slope, the energy budget greatly changes except for in the initial time, during which the slope angle has little effect on the energy budget. After that, at an identical time in the development of the turbidity current, the increase of θ brings a larger E_k and a smaller E_p . The overall tendency of E_k changes into a continuous increase process. When the slope angle gets larger, the increase tendency of E_k also becomes more obvious, which corresponds to the variation of U_f . The larger E_k and smaller E_p demonstrate that the increase of the slope angle can lead to a more rapid energy transition process of the turbidity current. On the other hand, the change of slope angle seems to influence the dissipated energy irregularly.

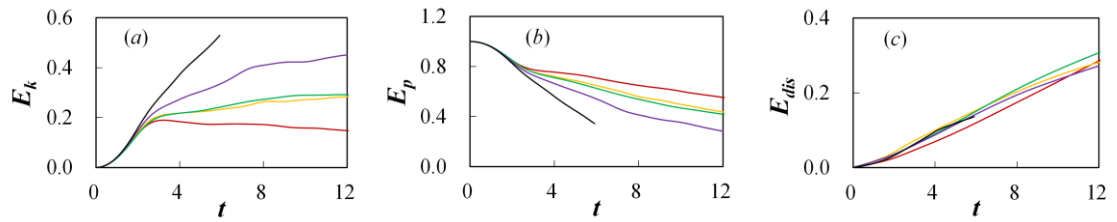


Fig. 16. Time evolution of (a) kinetic energy, (b) available potential energy and (c) dissipated energy of turbidity currents down different slopes. $Re = 3000$. —, $\theta = 0^\circ$; —, $\theta = 6^\circ$; —, $\theta = 10^\circ$; —, $\theta = 15^\circ$; —, $\theta = 30^\circ$. These energy terms are normalized by the initial potential energy $E_p(0)$.

5. Conclusions

Although gravity and turbidity currents play an important role in many aspects of natural processes and engineering practice, until now, there are still few studies which consider the effect of both the slope and particle on the development of the lock-exchange turbidity currents. This study presents two-dimensional direct numerical simulations of lock-exchange turbidity currents propagating within a relatively small slope range ($\theta \leq 30^\circ$). The accuracy of the numerical model is validated by comparing the simulation results with the data obtained in the published literature. With the high-resolution information of the spatio-temporal flow field, the development process, the front velocity, the entrainment ratio, and the energy budget of the turbidity current are detailedly analyzed. We investigate the influence of the settling velocity and the slope angle on the characteristics of the turbidity currents.

The simulation results show that, after the particle-laden fluid is released from a rest state, it rapidly starts to collapse forward and a leading head is then formed. The basic features, such as the Kelvin–Helmholtz instabilities, the turbulent billows, and the lifted nose at the lower boundary, can be well reproduced by our numerical model. The front velocity history presents three distinct stages. At the initial time, the collapse of the dense fluid leads to a short acceleration stage of the turbidity current, during which its front velocity increases rapidly from zero to the maximum value. At this stage, as the motion of the current is mainly dominated by the collapse of the particle-laden fluid, the influence factors mentioned above have little effect on the features of the turbidity current. Later, a temporary balance is achieved between the negative effects and the positive effect which both alter the driving force. Therefore, the turbidity current enters into a quasi-constant stage and U_f keeps a nearly constant value. Then, as the component of the reduced gravitational force is not large enough to make up the negative effects, the turbidity current starts to decelerate. Under the effect of particle settling and mixing with ambient lighter fluid, the density of the current is continuously reduced and the turbidity current finally dies out by the viscous effect. For the relatively small Reynolds number, $Re < 1000$, the increase of Re can bring a larger U_f . This dependence relationship can be neglected when $Re > 1000$. The analysis of the settling velocity shows that the turbidity current containing coarse particles loses particles more quickly, leading to an obvious decrease of U_f . The slope can bring a component of the reduced gravitational force along the slope,

the increase of θ leads that the tendency of U_f in the quasi-constant stage alters from the slight decrease to minor increase. When the slope angle gets larger, the increase tendency of U_f in the quasi-constant stage becomes more obvious.

Based on the volume change and the front velocity, the bulk and local entrainment ratios of the turbidity current are investigated. In the acceleration stage, the collapse of the dense fluid makes the ambient lighter water move along another direction, which promotes the mixing and entrainment effect. E_{bulk} and E_{local} of the turbidity current rapidly drops in this initial time period. Later then, E_{bulk} keeps a nearly constant value of the order of 10^{-2} . However, the behavior of E_{local} is much more complicated. The vigorous time variation of E_{local} is exactly the result of the irregular development of the Kelvin–Helmholtz instabilities and turbulent billows at the upper interface. The existence of the slope can bring a larger E_{bulk} , making more ambient lighter fluid entrained into the current. The huge difference of the entrainment ratio in the initial and later time proves that the mixing and entrainment due to the collapse of the dense fluid is much stronger than that due to the turbulent structures. For a turbidity current down a slope, the entrainment volume of the ambient water decreases as the particle size increases, which is contrary to the situation of the turbidity current on a flat bed. This is because the increase effect of the larger front velocity exceeds the decrease effect of the stronger stratification to the entrainment volume of the ambient water. On the other hand, the particle size has little effect on E_{bulk} and E_{local} of a turbidity current down a slope.

The near constant value of the total energy proves that the energy budget equation derived in this paper can be well applied to describe the energy change process of the turbidity current down a slope. In the initial stage, the potential energy E_p is rapidly converted into the kinetic energy E_k . The turbidity current gets most of its final E_k within this short time. After this, most of E_p is transformed into the dissipated energy E_{dis} , during which E_k grows slowly. Although the change of the particle size does not alter the overall tendency of E_k , E_p and E_{dis} , the increase of the particle size makes the energy dissipated more quickly, resulting in smaller E_k and E_p . At an identical time in the development of the turbidity current, the increase of θ brings a larger E_k and a smaller E_p , which means that a more rapid energy transition process of the turbidity current is presented. Despite the present two-dimensional DNS can get many features of the turbidity current down a slope, the

three-dimensional DNS is still needed to obtain the spanwise information of the turbidity current down a slope in the future.

Acknowledgement

References

- [1] Simpson J E. Gravity currents in the laboratory, atmosphere, and ocean[J]. *Annual Review of Fluid Mechanics*, 1982,14(1):213-234.
- [2] Meiburg E, Radhakrishnan S, Nasr-Azadani M. Modeling Gravity and Turbidity Currents: Computational Approaches and Challenges[J]. *Applied Mechanics Reviews*, 2015,67(4):40802.
- [3] Ho H, Lin Y. Gravity currents over a rigid and emergent vegetated slope[J]. *Advances in Water Resources*, 2015,76:72-80.
- [4] Hu P. Coupled modelling of turbidity currents over erodible beds[D]. Edinburgh: Heriot-Watt University, 2012.
- [5] Meiburg E, Kneller B. Turbidity Currents and Their Deposits[J]. *Annual Review of Fluid Mechanics*, 2010,42(1):135-156.
- [6] Huppert H E, Simpson J E. The slumping of gravity currents[J]. *Journal of Fluid Mechanics*, 1980,99(04):785-799.
- [7] Beghin P, Hopfinger E J, Britter R E. Gravitational convection from instantaneous sources on inclined boundaries[J]. *Journal of Fluid Mechanics*, 1981,107:407-422.
- [8] Maxworthy T, Nokes R I. Experiments on gravity currents propagating down slopes. Part 1. The release of a fixed volume of heavy fluid from an enclosed lock into an open channel[J]. *Journal of Fluid Mechanics*, 2007,584:433-453.
- [9] Dai A. Experiments on gravity currents propagating on different bottom slopes[J]. *Journal of Fluid Mechanics*, 2013,731:117-141.
- [10] Dai A. High-resolution simulations of downslope gravity currents in the acceleration phase[J]. *Physics of Fluids*, 2015,27(7):76602.
- [11] Dai A, Huang Y. High-resolution simulations of non-Boussinesq downslope gravity currents in the acceleration phase[J]. *Physics of Fluids*, 2016,28(2):26602.
- [12] Chadha T. Numerical study on particle sedimentation and deposition in turbidity currents[D]. ETH ZURICH, 2015.
- [13] Turner J S. Turbulent entrainment: the development of the entrainment assumption, and its application to geophysical flows[J]. *Journal of Fluid Mechanics*, 1986,173:431-471.
- [14] Hu P, Pätz T, He Z. Is it appropriate to model turbidity currents with the three - equation model?[J]. *Journal of Geophysical Research: Earth Surface*, 2015,120(7):1153-1170.
- [15] Parker G, Fukushima Y, Pantin H M. Self-accelerating turbidity currents[J]. *Journal of Fluid Mechanics*, 1986,171:145-181.
- [16] Krug D, Holzner M, Lüthi B, et al. Experimental study of entrainment and interface dynamics in a gravity current[J]. *Experiments in Fluids*, 2013,54(5):1-13.
- [17] Hallworth M A, Huppert H E, Phillips J C, et al. Entrainment into two-dimensional and axisymmetric turbulent gravity currents[J]. *Journal of Fluid Mechanics*, 1996,308:289-311.

- [18] Nogueira H I, Adduce C, Alves E, et al. Dynamics of the head of gravity currents[J]. *Environmental Fluid Mechanics*, 2014,14(2):519-540.
- [19] Ottolenghi L, Adduce C, Inghilesi R, et al. Entrainment and mixing in unsteady gravity currents[J]. *Journal of Hydraulic Research*, 2016:1-17.
- [20] Ottolenghi L, Adduce C, Inghilesi R, et al. Mixing in lock-release gravity currents propagating up a slope[J]. *Physics of Fluids*, 2016,28(5):56604.
- [21] Necker F, Härtel C, Kleiser L, et al. High-resolution simulations of particle-driven gravity currents[J]. *International Journal of Multiphase Flow*, 2002,28(2):279-300.
- [22] Huang H, Imran J, Pirmez C. Numerical model of turbidity currents with a deforming bottom boundary[J]. *Journal of Hydraulic Engineering - ASCE*, 2005,131(4):283-293.
- [23] Huang H, Imran J, Pirmez C. Numerical study of turbidity currents with sudden-release and sustained-inflow mechanisms[J]. *Journal of Hydraulic Engineering - ASCE*, 2008,134(9):1199-1209.
- [24] Abd El Gawad S, Cantelli A, Pirmez C, et al. Three-dimensional numerical simulation of turbidity currents in a submarine channel on the seafloor of the Niger Delta slope[J]. *Journal of Geophysical Research: Oceans*, 2012,117(C5):C5026.
- [25] Guo Y, Zhang Z, Shi B. Numerical Simulation of Gravity Current Descending a Slope into a Linearly Stratified Environment[J]. *Journal of Hydraulic Engineering - ASCE*, 2014,140(12):4014061.
- [26] Ooi S K, Constantinescu G, Weber L. Numerical simulations of lock-exchange compositional gravity current[J]. *Journal of Fluid Mechanics*, 2009,635:361-388.
- [27] An S, Julien P Y, Venayagamoorthy S K. Numerical simulation of particle-driven gravity currents[J]. *Environmental fluid mechanics*, 2012,12(6):495-513.
- [28] Tokyay T, Constantinescu G, Meiburg E. Lock-exchange gravity currents with a high volume of release propagating over a periodic array of obstacles[J]. *Journal of Fluid Mechanics*, 2011,672:570-605.
- [29] Tokyay T, Constantinescu G, Meiburg E. Lock-exchange gravity currents with a low volume of release propagating over an array of obstacles[J]. *Journal of Geophysical Research: Oceans*, 2014,119(5):2752-2768.
- [30] Tokyay T, Constantinescu G. The effects of a submerged non-erodible triangular obstacle on bottom propagating gravity currents[J]. *Physics of Fluids*, 2015,27(5):56601.
- [31] Härtel C, Meiburg E, Necker F. Analysis and direct numerical simulation of the flow at a gravity-current head. Part 1. Flow topology and front speed for slip and no-slip boundaries[J]. *Journal of Fluid Mechanics*, 2000,418:189-212.
- [32] Necker F, Härtel C, Kleiser L, et al. Mixing and dissipation in particle-driven gravity currents[J]. *Journal of Fluid Mechanics*, 2005,545:339-372.
- [33] Liu X, Jiang Y. Direct numerical simulations of boundary condition effects on the propagation of density current in wall-bounded and open channels[J]. *Environmental Fluid Mechanics*, 2014,14(2):387-407.
- [34] Blanchette F, Strauss M, Meiburg E, et al. High - resolution numerical simulations of resuspending gravity currents: Conditions for self - sustainment[J]. *Journal of Geophysical Research: Oceans (1978 - 2012)*, 2005,110(C12).
- [35] Dai A. Gravity currents propagating on sloping boundaries[J]. *Journal of Hydraulic Engineering - ASCE*, 2013,139(6):593-601.

- [36] Nasr-Azadani M M, Meiburg E. Influence of seafloor topography on the depositional behavior of bi-disperse turbidity currents: a three-dimensional, depth-resolved numerical investigation[J]. *Environmental Fluid Mechanics*, 2014,14(2):319-342.
- [37] Nasr-Azadani M M, Meiburg E. Turbidity currents interacting with three-dimensional seafloor topography[J]. *Journal of Fluid Mechanics*, 2014,745:409-443.
- [38] Espath L, Pinto L C, Laizet S, et al. Two-and three-dimensional Direct Numerical Simulation of particle-laden gravity currents[J]. *Computers & Geosciences*, 2014,63:9-16.
- [39] Osher S, Fedkiw R. *Level set methods and dynamic implicit surfaces*[M]. Berlin: Springer, 2006.
- [40] Jiang G, Peng D. Weighted ENO schemes for Hamilton--Jacobi equations[J]. *SIAM Journal on Scientific computing*, 2000,21(6):2126-2143.
- [41] Yu C, Wang D, He Z, et al. An optimized dispersion-relation-preserving combined compact difference scheme to solve advection equations[J]. *Journal of Computational Physics*, 2015,300:92-115.
- [42] Chorin A J. Numerical solution of the Navier-Stokes equations[J]. *Mathematics of computation*, 1968,22(104):745-762.
- [43] Choi J, Oberoi R C, Edwards J R, et al. An immersed boundary method for complex incompressible flows[J]. *Journal of Computational Physics*, 2007,224(2):757-784.
- [44] Kubo Y. Experimental and numerical study of topographic effects on deposition from two-dimensional, particle-driven density currents[J]. *Sedimentary Geology*, 2004,164(3):311-326.
- [45] Birman V K, Meiburg E, Ungarish M. On gravity currents in stratified ambients[J]. *Physics of Fluids*, 2007,19(8):86602.
- [46] Ellison T H, Turner J S. Turbulent entrainment in stratified flows[J]. *Journal of Fluid Mechanics*, 1959,6(3):423-448.
- [47] Wells M, Nadarajah P. The Intrusion Depth of Density Currents Flowing into Stratified Water Bodies[J]. *Journal of Physical Oceanography*, 2009,39(8):1935-1947.
- [48] Nasr-Azadani M M, Meiburg E, Kneller B. Mixing dynamics of turbidity currents interacting with complex seafloor topography[J]. *Environmental Fluid Mechanics*, 2016:1-23.